Nuclear Instruments and Methods in Physics Research A 740 (2014) 257–265

Contents lists available at ScienceDirect

Nuclear Instruments and Methods in Physics Research A

journal homepage: www.elsevier.com/locate/nima

High energy electrons from interaction with a structured gas-jet at FLAME

G. Grittani [a,b,c,*], M.P. Anania [d], G. Gatti [d], D. Giulietti [a,b,c], M. Kando [e], M. Krus [f], L. Labate [a,b], T. Levato [a,f], P. Londrillo [g], F. Rossi [g], L.A. Gizzi [a,b]

[a] ILIL, Istituto Nazionale di Ottica, CNR, Via G. Moruzzi 1, Pisa, Italy
[b] INFN Sezione di Pisa, Largo Pontecorvo 3, 56127 Pisa, Italy
[c] Dipartimento di Fisica E. Fermi, Universitá di Pisa, Italy
[d] Laboratori Nazionali di Frascati, INFN, Via E. Fermi, Frascati, Italy
[e] Japan Atomic Energy Agency (JAEA), Kyoto, Japan
[f] Institute of Physics of the ASCR, ELI-Beamlines project, Na Slovance 2, 18221 Prague, Czech Republic
[g] Universitá di Bologna e sez. INFN, Bologna, Italy

ARTICLE INFO

Available online 14 November 2013

Keywords:
Beam-plasma interactions
Laser-plasma acceleration
Ultra-intense laser–matter interaction

ABSTRACT

In this paper we analyze the properties of the electron bunches produced in a laser-plasma acceleration experiment using a 10 mm helium gas-jet with a longitudinal density profile characterized by a double peak structure. Data were taken at three different gas-jet backing pressures of 5, 8 and 15 bars, corresponding to plasma densities of $1.2–3.6 \times 10^{19}\,cm^{-3}$ in the peaks and $3.5–10 \times 10^{18}\,cm^{-3}$ in the central plateau. The highest energy peak is recorded at more than 450 MeV, with average energies between 80 and 180 MeV. Bunch divergence and pointing stability have been measured and are found to be very sensitive to the density. Fully 3D PIC numerical simulations confirm that laser intensity and plasma density of our set up are in the range where electron acceleration takes place by self-injection in a bubble-like structure. Analysis shows that after the first density peak, accelerated electrons propagate through the plateau and the second density peak without the driver, undergoing non-linear interaction with the background plasma.

1. Introduction

The production of ultrarelativistic electron bunches in a few-mm acceleration length is nowadays routinely done in laser laboratories all over the world, after the breakthrough [1–3] achieved using the Laser Wakefield Acceleration [4]. The wide range of possible applications of these bunches, from the radiotherapy to the fundamental physics, is actually leading to the realization of new laser facilities, as the Extreme Light Infrastructure (ELI) or to the upgrading of current laser facilities for dedicated studies [5].

Important issues in this context are the details of propagation [6] and ionization [7,8] of the laser pulse in the gas and the transport of accelerated electrons in the plasma beyond the acceleration region. These studies are also relevant for the physics of beam–plasma interaction for the development of particle wakefield accelerators [9]. Identification of dominant processes is crucial to improve stability and reliability of these high energy electron accelerators. In the case of laser driven acceleration, the best-suited regime to accelerate electrons is the so-called *bubble regime* [10], where an ultra-high intensity laser is focused in an underdense plasma and its ponderomotive force pushes away the electrons creating a bubble-like cavity. In the so-called self-injection [11] scheme, electrons originating from the plasma background are driven into this cavity and are accelerated by electric fields of the order of 100 GV/m. Since self-injection is experimentally accessible with relatively small laser systems, it has been extensively studied and many schemes to enhance it have been proposed in the past years, using magnetic fields [12] or density gradients [13], and many other [14]. A typical target consists of a gas-jet ejected from a Laval nozzle at a supersonic speed. Different techniques have also been developed to obtain more stable gas density profiles, such as the use of capillaries [15] or gas cells [16].

In this paper we describe and discuss recent results obtained using the FLAME (Frascati Laser for Acceleration and Multidisciplinary Experiments) laser [17] in the framework of the self-injection acceleration programme, aimed at establishing the specifications of self-injected bunches required for the on-going γ-ray source development [18] based upon the Thomson

* Corresponding author at: Institute of Physics of the ASCR, ELI-Beamlines project, Na Slovance 2, 18221 Prague, Czech Republic.
E-mail address: GabrieleMaria.Grittani@eli-beams.eu (G. Grittani).

0168-9002/$ - see front matter © 2013 Elsevier B.V. All rights reserved.
http://dx.doi.org/10.1016/j.nima.2013.10.082

scattering [19,20]. In those experiments, a gas-jet target was generated by a rectangular nozzle of 10 mm × 4 mm (Nitrogen) or 10 mm × 1.2 mm (Helium). Laser propagation was set to be either longitudinal (along the 10 mm side) or transverse (along the 4 mm or 1.2 mm sides). The transverse density profile is characterized by a rather typical "bell" shape, and laser acceleration in this profile was extensively explored numerically [21] and partially confirmed by preliminary measurements [18,22]. In contrast, the 10 mm long gas-jet is characterized by a structured longitudinal profile consisting of a double-peak density profile along the laser propagation axis. Propagation along the double-peaked, 10 mm density profile was therefore investigated to explore the possibility of future schemes of staged acceleration and to primarily investigate laser and electron propagation in such a structured plasma profile, with the first part of the profile acting as the accelerating region and the second part acting as a target plasma for the accelerated bunch. Here we describe the first data obtained in this configuration, with particular attention to the characterization of the accelerated bunch and to the properties of the target plasma. Finally we discuss the scenario emerging in our experimental conditions, also with the aid of 3D PIC (particle-incell) simulations.

2. Experimental set-up

FLAME is a nominal 220 TW laser system that uses 11 YAG pump lasers and 5 titanium-sapphire multi-pass amplifiers to produce linearly polarized pulses with a central wavelength of $\lambda_0 = 0.805$ μm, pulse duration of $\tau_L \leq 30$ fs and maximum energy > 7 J at a 10 Hz repetition rate. The laser system is hosted in a clean room at the ground floor and is then optically transported in a shielded underground target area, where it is focused via an f/10 off-axis parabolic mirror in a 15 μm diameter (FWHM) spot inside the vacuum chamber. Fig. 1 shows schematically the experimental set-up in the proximity of the target chamber. The vacuum chamber is 80 cm in diameter and during the experiment is kept at less than 10^{-8} bars. The nozzle, located at the center of the target chamber, ejects supersonic gas-jets. In this experiment the backing pressure was set in the range from 5 to 15 bars using a pressure gauge. The nozzle is mounted on a 3D micro-motor system used for the alignment relative to the laser focal spot position. Assuming full ionization, plasma density profile on the axis along the 10 mm length consists of two peaks and a central plateau as shown in Fig. 2 in the case of 5 bars backing pressure. The density profile was obtained [24] using a Mach-Zehnder interferometer to measure the phase shift due to the refractive index of the neutral gas. Ar was used for the measurements due to its higher refractive index (1.000283) compared to He (1.000035) which makes it easier to detect fringe shifts in the interferometry.

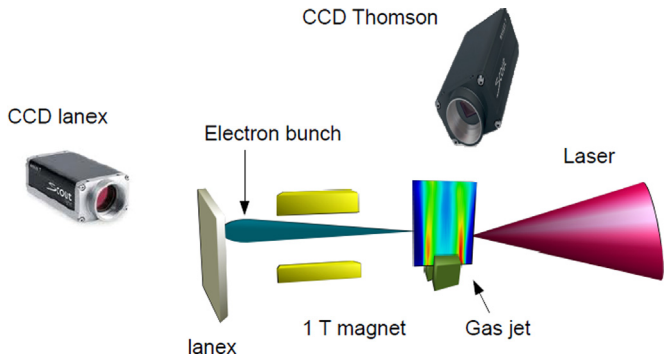

Fig. 1. Scheme of the experimental set up showing the main diagnostics including the scintillating screen for electron spectra, divergence and stability, and the Thomson scattering imaging. We used Basler Scout cameras [23] for imaging.

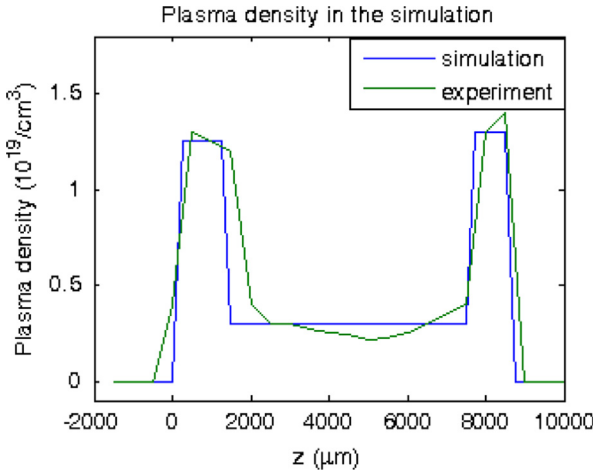

Fig. 2. Plasma density profile in the case of full ionization at a backing pressure of 5 bars used for the simulations (blue) compared with the experimental values (green) extrapolated from Ref. [24]. (For interpretation of the references to color in this figure caption, the reader is referred to the web version of this article.)

Since the nozzle design depends mainly upon the type of gas used (monoatomic or diatomic), via the ratio of the heat capacities C_p/C_v, a similar profile is expected for other monoatomic gases including He. According to this profile, at the backing pressure of 10 Bars, the maximum atom density in the profile is approximately 1.2×10^{19} cm^{-3}, while the plateau has a density between 3×10^{18} and 4×10^{18} cm^{-3}, namely a factor of 3–4 less than the peak density. These values scale linearly with the backing pressure and therefore for the lowest pressure of 5 Bar we expect a peak and a plateau average atom densities of 6×10^{18} cm^{-3} and 1.75×10^{18} cm^{-3} respectively, while for the 15 Bar pressure these values become 1.8×10^{19} cm^{-3}and 5.2×10^{18} cm^{-3} respectively.

A scintillator crystal (NaI(Tl)) coupled with a PMT is placed outside the target chamber to detect gamma-ray signal which is mainly due to the interaction of the accelerated electrons with the chamber walls. A 5 cm long magnetic dipole of nominal field intensity of 1 T is placed along the propagation axis. It is mounted on a 1D motorized slide in order to allow remote control of the extraction of the magnet on the beam for bunch divergence and pointing stability measurements. A Lanex scintillating screen is placed on axis attached to the inner face of a glass window of the chamber. The screen emits green light proportional to the energy deposited by the incident electrons. The light is collected by a lens and imaged onto a CCD outside the chamber. We also detect images of the Thomson scattered radiation emitted in the direction perpendicular to the laser polarization plane during laser propagating inside the gas. We use a lens to image the plasma on a color CCD so that Thomson scattering radiation can be easily separated from plasma self-emission [25]. For the data shown here, the laser intensity on target was $I_0 = 2 \times 10^{19}$ W/cm^2, which corresponds to a normalized vector potential $a_0 = 3.4$. Two series of data have been acquired during the experiment:

- *pointing shots*, with the magnet out of the electrons trajectory, to study the bunch divergence and pointing stability
- *spectrum shots*, with the magnet along the electrons path, to study the spectrum of the bunch and the divergence along the non-dispersive axis.

For each of these shots, a Thomson scattering image was also taken. An example of Thomson scattering image is displayed in Fig. 3 where the laser propagates from the left. The image clearly shows on the left an orange-red emission due to Thomson scattering from laser propagation inside the gas-jet. As discussed

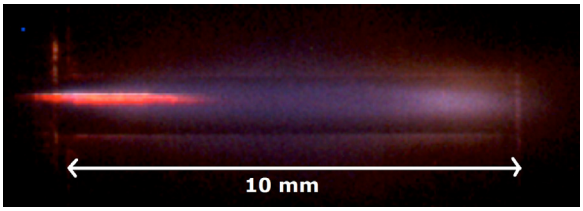

Fig. 3. Example of Thomson scattering image taken at 8 bar. The laser impinges from the left and the Thomson scattered radiation is clearly visible (orange-red). Self-emission from the plasma is also visible in the background (For interpretation of the references to color in this figure caption, the reader is referred to the web version of this article.).

below, information about the laser depletion length is taken from the length of the Thomson scattering emitting region as discussed in Ref. [25]. In addition, a diffuse blue emission is also visible, most likely due to plasma self-emission. It should be noted that the plasma self emission occurs at later times, typically nanoseconds after the passage of the laser pulse in the gas, but since our CCD collects light over a much longer time (typically few ms) both emission components appear superimposed on the image. We observe that the presence of plasma self-emission is a signature of plasma recombination and deexcitation following laser induced ionization. The darker region in the middle corresponds to the low density plateau of the density profile. These images give us an estimate of the propagation length inside the gas-jet, which is an important parameter for the simulations.

As for electron bunch measurements, a total of 369 pointing images have been taken: including 42 shots at 5 bars, 137 shots at 8 bars and 190 shots at 15 bars. In these images we have seen either spray of electrons or one or more collimated few-mrad bunches. The transition between spray and collimated bunch was found to be very sharp when moving the focal spot along the gas target by a few hundreds of μm. For each Lanex image we obtain the charge [26] of the incident electron bunch. We find that the charge measured in these images fluctuated over 2 orders of magnitude at a given pressure. The crucial parameters to be evaluated in this phase are the divergence of the bunch and its pointing stability. The resolution of our acquisition system is limited by the area of the Lanex screen corresponding to each pixel of the imaging system, which is 0.7 mrad for the y divergence (vertical axis of the lanex screen) and 0.6 mrad for the x divergence (horizontal axis of the lanex screen).

3. Bunch divergence

Bunch divergence is defined here as the full angular aperture of the bunch, evaluated considering the FWHM of the intensity distribution of the image on the Lanex screen. In the case of multiple bunches, this measurement was carried out twice: first considering only the most intense of the bunches, and after considering all the multiple bunches. Multi-bunch divergence is 20 mrad along the axis parallel to laser polarization axis ($\hat{x}$) and 14 mrad along the vertical axis ($\hat{y}$), thus it is 3–5 times higher than the divergence of a single bunch. The divergence has been evaluated on both x and y and the standard deviation of the data set has been taken as uncertainty on the measurements. Fig. 4 shows the histogram of the vertical divergences relative to the case of 15 bars. Histograms relative to the other pressures show similar shape. As shown in the Fig. 4, divergences were almost stable in 2–8 mrad region with occasional higher and lower (up to 1 mrad) occurrences. Results are summarized in Table 1. At 8 bars the divergence is slightly lower than in the case of 15 bars, while at 5 bars the divergence is one order of magnitude higher. These few

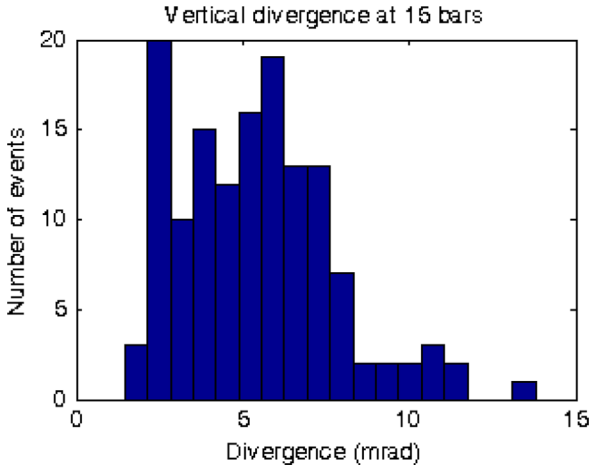

Fig. 4. Histogram of the vertical full-angle divergence of the bunches accelerated at 15 bars backing pressure.

Table 1
Average bunch divergences at different backing pressures.

Pr. (bar)	Div. X (mrad)	Div. Y (mrad)
5	77 ± 21	74 ± 18
8	4.8 ± 3.4	4.8 ± 3.6
15	4.9 ± 3.2	5.3 ± 2.4

Table 2
Beam pointing at different backing pressures.

Pr. (bar)	Point. X (mrad)	Point. Y (mrad)
5	2.9 ± 0.2	1.5 ± 0.2
8	18.7 ± 0.9	17.2 ± 1.6
15	11.1 ± 0.6	9.1 ± 0.8

mrad divergences are similar to the estimated 10 mrad in a preliminary run at FLAME [27] and with other experiments in similar regimes [28].

4. Pointing stability

Stability of the pointing has been evaluated considering the intensity peak of the collimated bunch, taking the position and considering the standard deviation of the data set as pointing error, as the positions exhibit an almost Gaussian distribution. At 15 bars multiple bunches were detected by the Lanex screen for a half of the shots, in these cases only the brightest bunch signal, closest to the average pointing, was considered. The uncertainty on the pixel size is taken as the uncertainty on the pointing measure. Results are reported in Table 2. At 8 and 15 bars we observe a pointing instability higher than the bunch divergence, which is in agreement with [28]. At 5 bars we observe the best stability, while at 8 bars we find the less stable pointing. These results are summarized in Fig. 5. We observe that in all the three cases, the spread of the pointing along the vertical direction is lower (more stable) than that along the horizontal direction, namely in the laser polarization plane. This observation, along with the measurement of multi-bunch divergence, suggests that the laser electric field may be playing a role in setting the transverse momentum of the accelerated electron bunch. This effect is more pronounced at the highest electron density, where a clear preferential direction of spreading is observed at an angle of

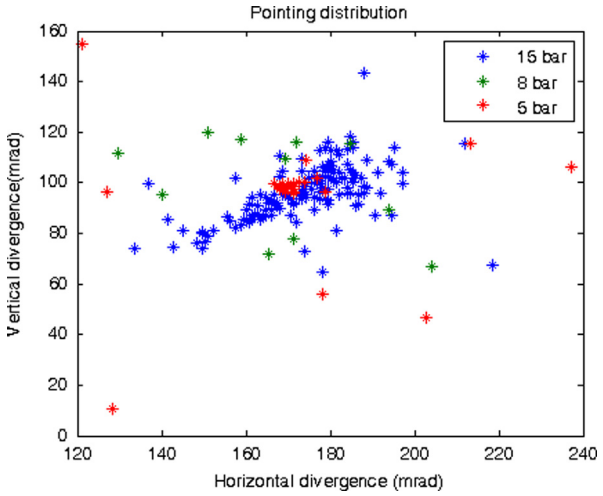

Fig. 5. Pointing position of all the shots taken.

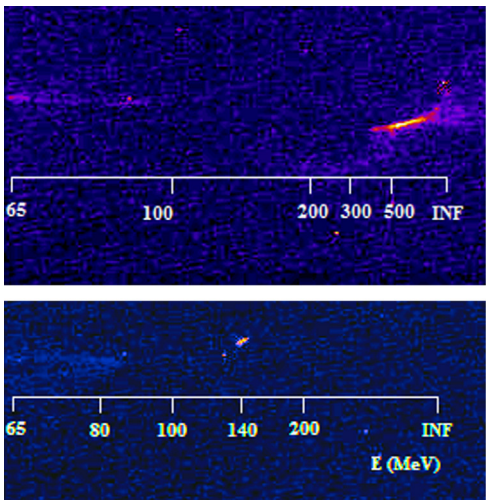

Fig. 6. Upper image: Electron spectrum obtained at 8 bars, showing a cut-off energy above 450 MeV (see text). Lower image: Electron spectrum obtained showing the lowest energy spread (4.6 %), obtained again at 8 bars.

approximately 40° from the horizontal (polarization) plane. A dependence on the laser polarization was observed earlier [29] on the ellipticity of the bunch. In those measurements, the ellipticity was found to appear for plasma density such that $c\tau \simeq \lambda_p$, where τ is the laser pulse duration and λ_p is the plasma wavelength. Here, a similar effect is found on the spread of pointing, while the measurement of the ellipticity is not sufficiently accurate to show the same evidence. Among other possible mechanisms that could be invoked here, the hosing instability has been identified [14] as possible source of perturbation on the propagation trajectory of the laser pulse and of the accelerating bubble structure. This is seeded by an insufficiently smooth laser centroid in the focal spot and its growth is more effective at higher electron densities. However, theoretical and numerical studies on such non-axisymmetric instabilities in laser–plasma interaction depending on the laser polarization plane are still limited to particular cases of higher, near-critical densities [30]. In our simulation studies presented below, we observe hosing-like instabilities in the wake structure during the first acceleration stage limited to the first density peak, resulting in a higher bunch angular displacement on the polarization plane. At later stages of propagation in the density profile we observe the leading bunches overtaking the tail of the laser pulse and this could be a second source of polarization-dependent non-axisymmetric effects. However, these are only preliminary observation that call for further experimental investigation to identify the role of this instability in our measurements.

5. Electron spectra

Electron spectra have been evaluated integrating the strip on the non-dispersive axis and assigning to each pixel of the image the corresponding energy. These energies have been evaluated considering the motion of the electrons in a uniform magnetic field. These assumption has been verified experimentally by a direct measurement via hall probe and the field B_0 used for the calculations has been evaluated using the SCOFF approach [31,32]:

$$\frac{1}{l}\int_{-\infty}^{\infty} B(x)\,dx = B_0 \tag{1}$$

where l is the length of the magnet and B_0 is the constant field used for the calculations. Bunch electron spectra have been measured only at 8 bars and 15 bars pressures. Lanex screen was set perpendicular to the laser propagation axis, and due to its size, only electrons with energy higher than 64 MeV (at 8 bars) and 60 MeV (at 15 bars) were detectable. Furthermore, pointing instability and beam divergence evaluated previously, are the main source of uncertainty on the measured energy and define the maximum detectable energy, which turns out to be 450 MeV at 8 bars and 740 MeV at 15 bars. Fig. 6 shows images of two spectra, namely the highest energy and the lowest energy spread shots obtained in this data-set, after processing of the Lanex screen image and calibration.

Table 3
Bunch spectral properties measured at different backing pressures. Energies are in MeV and charge is in pC.

Pr. (bar)	E_{peak}	E_{mean}	Cut-off	Charge
8	150 ± 120	136 ± 62	450 ± 280	120 ± 60
15	110 ± 46	108 ± 25	370 ± 210	180 ± 100

For each spectrum we consider the peak energy (the energy of the brightest peak in the spectrum), the FWHM energy spread, the mean energy, the high energy cut-off (defined as the maximum energy whose signal is higher than 1/6 of the intensity peak) and the charge. The cut-off at 1/6 is motivated by the fact that in our data set this is the lowest ratio at which the corresponding signal is more than 3 times higher than the noise in each sample. Results are summarized in Table 3 and the reported uncertainties are the standard deviations of the data sets. According to the results of Table 3, the most energetic bunches were obtained at a pressure of 8 bars, while in the case of 15 bars we had higher charge. Moreover, at 15 bars we had more reproducible bunches, meaning that the standard deviation of the mean and peak energy is much lower than in the case of 8 bars. Furthermore, in the case of 15 bars we had 184 spectra over 200 shots, while with 8 bars we had only 87 spectra with the same number of shots, meaning that with 15 bars we had higher stability of bunch production. Average bunch energies are in a good agreement with the ones found in the preliminary run [27,36]. The highest peak bunch energy reached is more than 450 MeV, as shown in Fig. 6. The energy spread of the electron bunches was found to be smaller in the case of 8 bars, as shown by the histogram of Fig. 7(a), with a best shot obtained at 8 bars with an energy spread of 4.6% (Fig. 6). Fig. 7(b) also shows a typical electron spectrum obtained at 8 bars. Finally, the divergence of the non-dispersive axis vs. the energy of the electrons is

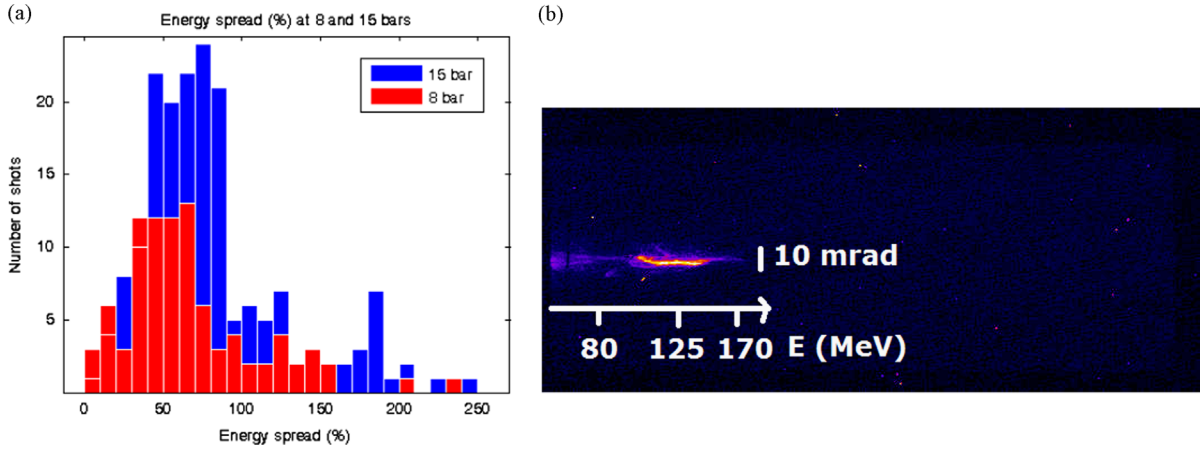

Fig. 7. (a) Energy spread at 8 (red) and 15 (blue) bars and (b) typical quasimonoenergetic bunch obtained at 8 bars. (For interpretation of the references to color in this figure caption, the reader is referred to the web version of this article.)

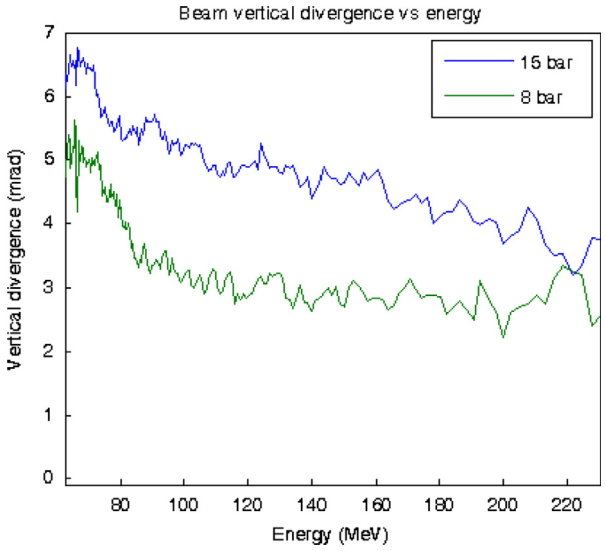

Fig. 8. Bunch vertical divergence vs. energy at 8 and 15 bars.

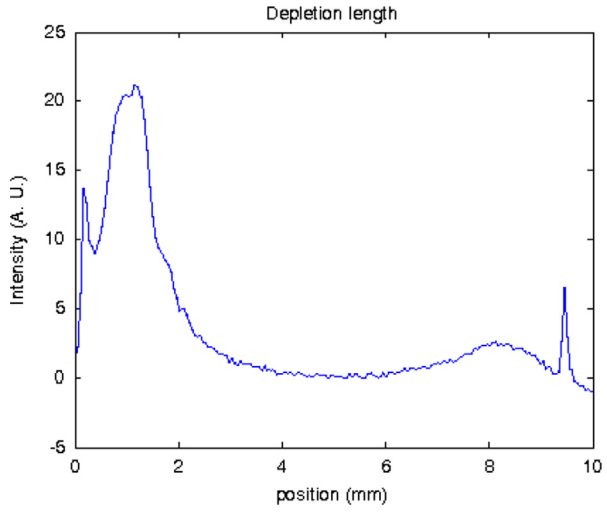

Fig. 9. Intensity profile of the red light integrated on the shorter side of the gas-jet.

shown in Fig. 8. The average divergence of the bunch plotted against the bunch energy shows that at 8 bars the bunch divergence is lower than in the case of 15 bars and, furthermore, that the higher energy electrons of the bunches are more collimated than the lower energy ones.

6. Thomson scattering images

As anticipated above, the laser depletion length has been estimated from the Thomson scattering images considering the length of the Thomson emission as visible in Fig. 2. Typically, Thomson emission was visible along the propagation of the laser light up to the transition from the first density peak and the central plateau. In this region the laser intensity is sufficiently high to give rise to full ionisation of the Helium atoms [7,8]. In view of this, depending on the backing pressure, the maximum density in the first peak will range between 1.2 and 3.6×10^{19} cm^{-3}. According to Fig. 3, the intensity of the Thomson scattered radiation rapidly drops as the laser propagates beyond the first density peak and only background plasma self-emission is visible from the density plateau and beyond. We point out that, since Thomson emission depends linearly on both the laser intensity and the electron density, the drop of the electron density profile (Fig. 2) by more than a factor of 3 in the plateau may affect this measurement, leading to an underestimation of the depletion length. However, over the entire dataset, no clear Thomson emission was detected beyond the first peak, even when strong saturation of the emission in the first peak occurred. These circumstances make us confident that the depletion length is mostly limited to the first peak of the density profile. A quantitative evaluation can be obtained by the Thomson emission profile of Fig. 9, by taking the width of the entire emission region. Standard deviation of the data set is taken as uncertainty and results of the analysis are reported in Table 4. This analysis shows that the depletion length, as derived from the Thomson scattering images, is weakly dependent upon the backing pressure, with the highest pressure of 15 bars giving a 5% shorter depletion length compared to the same length at 5 bars. Fluctuations of the depletion length from shot to shot are found to be of the same magnitude, as indicated by the statistical error in Table 4. We observe that this value of the depletion length is almost seven times the Rayleigh length of approximately 600 μm. Propagation over so many Rayleigh lengths implies a significant laser collimation, possibly with relativistic self-focusing balancing diffraction. Further discussion of the role of self-focusing is given below.

7. Discussion

The analysis of the bunch divergence shows a strong reduction from 5 to 8 bars, while it changes only slightly when passing from 8 to 15 bars. This, along with the fact that pointing stability is lower than the divergence only in the case of 5 bars, suggests that between 5 and 8 bars we can have a threshold between two different accelerating regimes. The study of bunch spectra shows that at 8 bars the bunches show higher peak, average and cut-off energies. Furthermore, at 8 bars peak energies are on average 10% higher than the mean energies, while in the case of 15 bars these are almost the same. Moreover, at 8 bars bunches shows significant lower energy spread than at 15 bars. All these observations consistently suggest that at 8 bars better conditions for self-injection are achieved. Measurements of divergence on the non-dispersive axis in the spectrum images show that at 8 bars bunches are more collimated than at 15, as anticipated by divergence measurements, and the divergence results to be lower at higher electron energy. Finally, Thomson images show laser depletion ranging from 4.2 mm to 4.0 mm for the range of pressures explored. This weak dependence on the gas density is currently being investigated as due to a combination of refraction and absorption effects. According to this general picture, since the depletion length is significantly smaller than the gas-jet length, the main acceleration is typically limited to the first density peak. The electrons accelerated in the first peak will propagate through the density plateau and the second peak where the laser intensity has dropped below the value required for driving the bubble. Also, due to the laser depletion, at this intensity, self-focusing driven light guiding effect will no longer occur and expansion of the laser beam after the focus will further reduce the intensity. However, even at less than one tenth of the initial laser intensity, i.e. around 10^{18} W/cm^2, He atoms will be singly ionized [7,8]. These circumstances are confirmed by the above observation concerning plasma self-emission from this region as visible from the Thomson scattering images. Therefore, in our experiment, the electron bunch accelerated in the first density peak, will first propagate in the plateau at an electron density ranging (for the three different backing pressures) approximately between 1.75 and 5×10^{18} cm^{-3} and in the second peak at electron densities between 6×10^{18} cm^{-3} and 1.8×10^{19} cm^{-3}. Table 5 summarizes

Table 4
Estimate of laser depletion length at different backing pressures.

Pr. (bar)	L (mm)
5	4.19 ± 0.21
8	4.10 ± 0.35
15	3.98 ± 0.37

Table 5
Expected values of the characteristic densities of the gas-jet along the laser bunch and propagation direction. Full ionization is assumed in the first peak and single ionization in the plateau and in the second peak.

Back. press. (bars)	1st peak max density (cm^{-3}) (full ion.)	Plat. avg. density (cm^{-3}) (He$^+$ ion.)	2nd peak max density (cm^{-3}) (He$^+$ ion.)
5	1.2×10^{19}	1.75×10^{18}	6.2×10^{18}
8	2×10^{19}	2.8×10^{18}	1.0×10^{19}
15	3.6×10^{19}	5.2×10^{18}	1.8×10^{19}

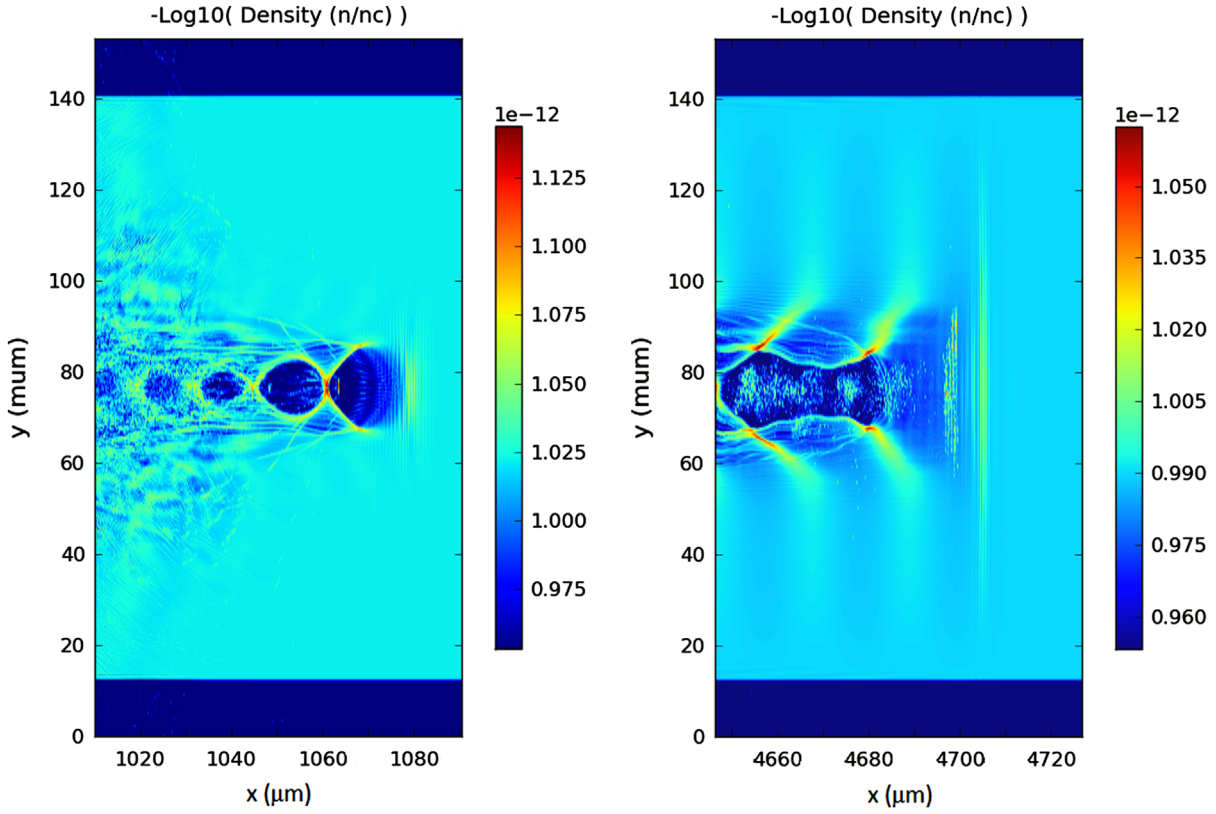

Fig. 10. Simulation of the electron acceleration at 5 bar. On the left we see that after the first mm of propagation, the laser pulse creates bubble cavities where electrons are self-injected and accelerated. On the right we see that when the laser is depleted (here 4.6 mm), bubbles break up with consequent loss of gain in kinetic energy for electrons.

the values of the densities for the entire profile, taking into account the expected ionization degree set by the laser propagation as discussed above.

Detailed study of propagation of our electron bunch in this plasma is a complex task and further investigation will be required to fully understand the propagation issues. As a preliminary step, 3D Particle-In-Cell simulations have been performed using the Jasmine [33] code to unfold the electron acceleration regime activated in the first peak and to calculate expected bunch properties at the exit of the first peak. A first simulation has been done considering a normalized vector potential $a_0=2.45$, laser waist size $w_0=15.5$ μm, laser pulse duration $\tau=30$ fs and the plasma density profile reported in Fig. 2, which refers to the case of 5 bar gas-jet backing pressure. Simulations show the formation of a bubble in the first density peak which then propagates through the plateau gradually losing its shape as the laser driver intensity decreases (see Fig. 10).

In the initial bubble, a bunch of electrons is self-injected and accelerated up to 242 MeV with a peak in the energy spectrum at 186 MeV with 6.1% relative energy spread (see Fig. 11). While the bubble loses its shape in the density plateau, the electron bunch partially loses energy and increases its divergence and its relative energy spread. Table 6 gives a comparison between bunch properties at 1 and 4, 7 mm propagation. According to these preliminary results, acceleration in the first density peak yields good quality bunches, with a small energy spread of 6% and horizontal and vertical divergences of 12 mrad and 9 mrad. Simulations also show that propagation in the plasma region with partial laser depletion strongly affects the quality of the bunch accelerated after the first density peak. In fact, the measured divergence is 5–7 times higher and no high energy electrons are observed.

As for the propagation in the remaining plasma region (plateau and second peak of the density profile), simulations results are still under scrutiny and additional work is needed. At this stage we can anticipate that at this density, simulations show the formation of a wake driven by a bunch propagating in the plateau. This is clearly visible in the density plot of Fig. 12. The laser pulse is visible at 6525 μm of propagation and at this stage has expanded to a diameter of ≈60 μm and so is the first electron bunch just behind. A second, moderately collimated bunch is located at 6505 μm and has created a strong wake just behind. A third, smaller bunch injected in this wake is also visible at 6495 μm. Simulation snapshots at later times (Fig. 12(right)) show that as the pulse propagates further and enters the second density peak, a partial refocusing of the residual laser light occurs, due to self-focusing, which drives a new bubble that accelerates additional electrons.

Clearly, these conditions will depend significantly upon the plasma density that will change the propagation and the acceleration conditions in the first peak and will affect bunch propagation in the plateau and in the second peak. To further clarify the role of density, we also carried out additional numerical simulations at higher densities than the one presented above. Indication from these simulations is that at higher densities, comparable to the maximum density explored experimentally, strong self-focusing occurs early in the propagation in the first density peak, with consequent strong defocusing and significant reduction of the acceleration length. On one hand, this makes the laser intensity in the plateau and the second density peak decrease more compared with the low density case discussed above, setting the conditions for a cleaner beam–plasma interaction, free from laser driven wakefield effects. On the other hand, the higher density makes acceleration in the first density peak less effective, with lower energy and broader spectrum. We are therefore driven to the conclusion that fine tuning of the plasma density may lead closer to the ideal situation of acceleration in the first density peak and beam–plasma interaction in the plateau and in the second density peak.

Indeed, assuming a bunch charge of 1 nC, a bunch duration of less than 6 fs [34] and a bunch radius of 5 μm, we find a bunch charge density greater than 4×10^{19} cm^{-3}. As discussed above,

Table 6
Bunch properties evaluated after the first mm and after 4.7 mm of propagation. The axis y is the polarization axis of the laser electric field.

Feature	1 mm	4.7 mm
Max energy (MeV)	242	346
Peak energy (MeV)	186	172
Energy spread (%)	6.1	14
Div$_y$ (mrad)	12.1	29.6
Div$_z$ (mrad)	8.7	18.1
Charge (pC)	86	163

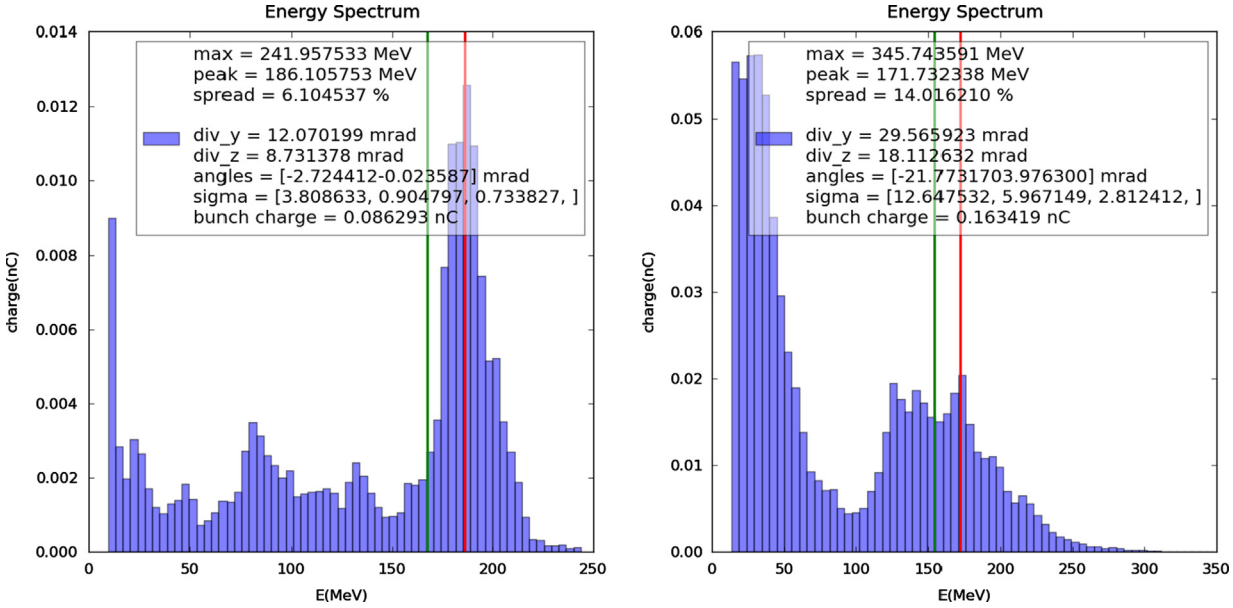

Fig. 11. Left: Electron bunch spectrum after the first density ramp. Right: Electron bunch spectrum after 4.6 mm of propagation.

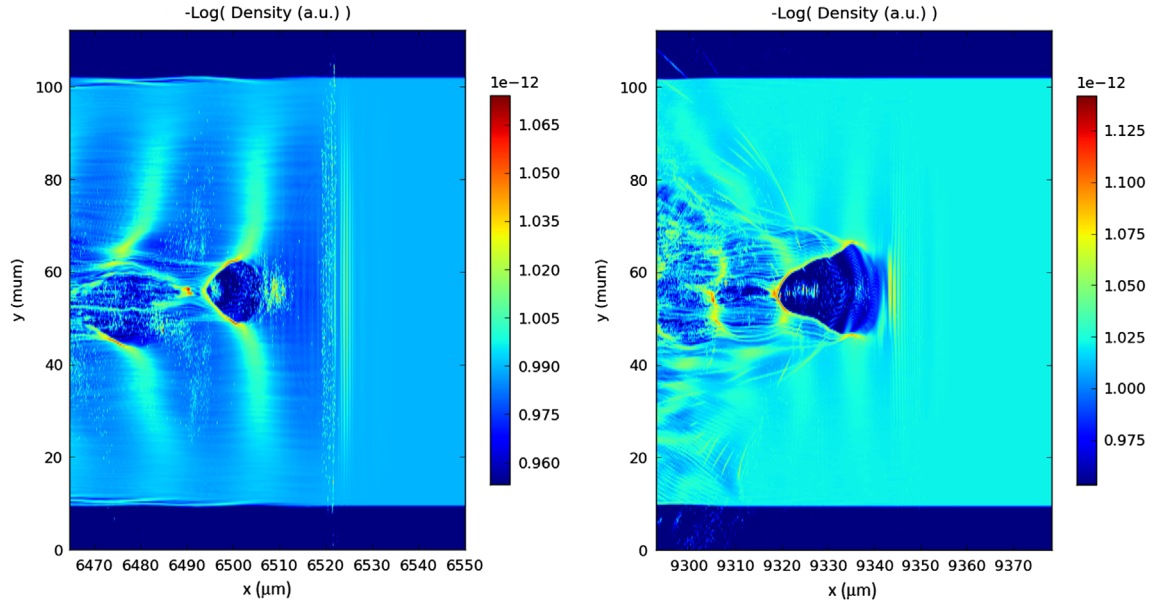

Fig. 12. Electron density plot obtained from simulations after 6525 μm (left) and 9350 μm (right) of propagation in the plateau and in the second density peak of the density profile. The wake produced by the electron bunch is visible in the left plot at 6505 μm.

this density is larger than the estimated density of the background plasma in the plateau ($< 5 \times 10^{18}$ cm^{-3}) as well as the density in the second peak (2×10^{19} cm^{-3}), setting the conditions for non-linear propagation of the bunch in the plasma [35]. These conditions are therefore expected to play an important role on the properties of the propagation of the accelerated bunch. This is consistent with the possible scenario predicted by simulations discussed above in which bunch will produce its own wakefields which will eventually slow down the bunch and affect the spectrum and the divergence, possibly via focusing fields. Also, given the partial ionization degree of the background plasma discussed above, as set by the laser propagation, the bunch could also give rise to additional ionization. A detailed analysis of this interaction is beyond the scope of this paper and is currently in progress. Here we would like to stress that, based on the characterization of our experimental conditions discussed in this paper, we confirm that our set up provides access to a range of beam–plasma parameters that are indeed relevant for studies of relativistic beam–plasma interaction.

8. Conclusions

We studied laser–plasma acceleration in a 10 mm long, double-peak density profile. We produced electron bunches with a few mrad divergences, typical peak energy of 150 MeV and energy spread of 45%. Record values for our data-set include shots with cut-off energies up to spectrometer resolution (450 MeV) and energy spread as small as 4.6%. Thomson scattering images shows that the laser depletes after less than half of the gas-jet length, with the bunch propagating in the remaining density profile with an attenuated laser pulse. 3D PIC simulations suggest that most of the acceleration indeed occurs in the first density peak, with broadening of the energy spectrum already occurring in the density plateau, where beam–plasma interaction, possibly in the non-linear regime, may also take place, ultimately setting the final bunch properties. Our results indicate that our set up can be tuned so that primary acceleration occurs only in the first density peak, leaving the remaining density profile free for non-linear beam–plasma interaction free from laser driven wakefield effects.

Acknowledgments

The Self-Injection Test Experiment (SITE) and the γ-ray Emitter from Self-Injected Thomson Scattering (γ-RESIST) are funded by INFN through the CN5. This work was carried out in collaboration with the High Field Photonics Unit at INO-CNR (MD.P03.034) and was partially funded by CNR through the ELI-Italy project. The work has been partially supported by the EU Commission in the Seventh Framework Program, Grant Agreement 312453 - EuCARD-2. We acknowledge the CINECA Grant N. HP10CZX6QK and IscrC_JA-BonB_E, 2013 for the availability of high performance computing resources and support. We acknowledge the support of INFN APE project for the availability of the QUonG cluster.

References

[1] S.P.D. Mangles, C.D. Murphy, Z. Najmudin, A.G.R. Thomas, J.L. Collier, A.E. Dangor, E.J. Divall, P.S. Foster, J.G. Gallacher, C.J. Hooker, D.A. Jaroszynski, A.J. Langley, W.B. Mori, P.A. Norreys, F.S. Tsung, R. Viskup, B.R. Walton, K. Krushelnick, Nature 431 (2004) 535.
[2] C.G.R. Geddes, C. Toth, J. van Tilborg, E. Esarey, C.B. Schroeder, D. Bruhwiler, C. Nieter, J. Cary, W.P. Leemans, Nature 431 (2004) 538.
[3] J. Faure, Y. Glinec, A. Pukhov, S. Kiselev, S. Gordienko, E. Lefebvre, J. Rousseau, F. Burgy, V. Malka, Nature 431 (2004) 541.
[4] T. Tajima, J.M. Dawson, Phys. Rev. Lett. 43 (1979) 267, http://dx.doi.org/10.1103/PhysRevLett.43.267, URL ⟨http://link.aps.org/doi/10.1103/PhysRevLett.43.267⟩.
[5] L. Labate, M. Andreassi, F. Baffigi, G. Basta, R. Bizzarri, A. Borghini, G. Candiano, C. Casarino, M. Cresci, F. Martino, L. Fulgentini, F. Ghetti, M. Gilardi, A. Giulietti, P. Köster, F. Lenci, T. Levato, Y. Oishi, G. Russo, A. Sgarbossa, C. Traino, L. Gizzi, Small-scale laser based electron accelerators for biology and medicine: a comparative study of the biological effectiveness, in: Proceedings of SPIE – The International Society for Optical Engineering 8779.
[6] A. Giulietti, P. Tomassini, M. Galimberti, D. Giulietti, L. Gizzi, P. Köster, L. Labate, T. Ceccotti, P. D'Oliveira, T. Auguste, P. Monot, P. Martin, Phys. Plasmas 13 (2006) 093103.
[7] L.A. Gizzi, S. Betti, M. Galimberti, A. Giulietti, D. Giulietti, L. Labate, T. Levato, P. Tomassini, P. Monot, T. Ceccotti, P. De Oliveira, P. Martin, Phys. Rev. E 79 (2009) 056405, http://dx.doi.org/10.1103/PhysRevE.79.056405, URL ⟨http://link.aps.org/doi/10.1103/PhysRevE.79.056405⟩.
[8] L.A. Gizzi, M. Galimberti, A. Giulietti, D. Giulietti, P. Koester, L. Labate, P. Tomassini, P. Martin, T. Ceccotti, P. De Oliveira, P. Monot, Phys. Rev. E 74 (2006) 036403, http://dx.doi.org/10.1103/PhysRevE.74.036403, URL ⟨http://link.aps.org/doi/10.1103/PhysRevE.74.036403⟩.
[9] I. Blumenfeld, C.E. Clayton, F.-J. Decker, M.J. Hogan, C. Huang, R. Ischebeck, R. Iverson, C. Joshi, T. Katsouleas, N. Kirby, W. Lu, K.A. Marsch, W.B. Mori, P. Muggli, E. Oz, R.H. Siemann, D. Walz, M. Zhou, Nature 445 (2007) 741.
[10] A. Pukhov, J.M. ter Vehn, Appl. Phys. B 74 (2002) 355.

[11] A. Oguchi, A. Zhidkov, T. Takano, E. Hotta, K. Nemoto, K. Nakajima, Phys. Plasmas 15 (2008) 043102.
[12] A. Zhidkov, T. Hosokai, S. Masuda, Y. Oishi, T. Fujii, R. Kodama, arXiv:1202.3828, 2012.
[13] S. Bulanov, N. Naumova, F. Pegoraro, J. Sakai, Phys. Rev. E 58 (1998) R5257, http://dx.doi.org/10.1103/PhysRevE.58.R5257, URL ⟨http://link.aps.org/doi/10.1103/PhysRevE.58.R5257⟩.
[14] E. Esarey, C.B. Schroeder, W.P. Leemans, Rev. Mod. Phys. 431 (2009) 538.
[15] S. Karsch, J. Osterhoff, A. Popp, T.P. Rowlands-Rees, Z. Major, M. Fuchs, B. Marx, R. Horlein, K. Schmid, L. Veisz, S. Becker, U. Schramm, B. Hidding, G. Pretzler, D. Habs, F. Gruner, F. Krausz, S.M. Hooker, New J. Phys. 9 (2007) 415.
[16] J. Osterhoff, A. Popp, Z. Major, B. Marx, T.P. Rowlands-Rees, M. Fuchs, M. Geissler, R. Horlein, B. Hidding, S. Becker, E.A. Peralta, U. Schramm, F. Gruner, D. Habs, F. Krausz, S.M. Hooker, S. Karsch, Phys. Rev. Lett. 101 (8) (2008) 085002.
[17] L. Gizzi, A. Bacci, S. Betti, C.A. Cecchetti, M. Ferrario, A. Gamucci, A. Giulietti, D. Giulietti, P. Koester, L. Labate, T. Levato, V. Petrillo, L. Serafini, P. Tomassini, C. Vaccarezza, Eur. Phys. J. Spec. Top. 175 (2009) 3.
[18] L.A. Gizzi, M.P. Anania, G. Gatti, D. Giulietti, G. Grittani, M. Kando, M. Krus, L. Labate, T. Levato, Y. Oishi, F. Rossi, Nucl. Instr. Methods Phys. Res. Sect. B: Beam Interact. Mater. Atoms 309 (2013) 202.
[19] P. Tomassini, A. Bacci, J. Cary, M. Ferrario, A. Giulietti, D. Giulietti, L. Gizzi, L. Labate, L. Serafini, V. Petrillo, et al., IEEE Trans. Plasma Sci. 36 (4) (2008) 1782.
[20] P. Tomassini, M. Galimberti, A.G.D. Giulietti, L.A. Gizzi, L. Labate, Phys. Plasmas 10 (2003) 917.
[21] L.A. Gizzi, F. Anelli, C. Benedetti, C.A.C.A. Clozza, G.D. Pirro, N. Drenska, R. Faccini, D. Filippetto, S. Fioravanti, A. Gamucci, D. Giulietti, L. Labate, T. Levato, V. Lollo, P. Londrillo, E. Pace, G. Turchetti, C. Vaccarezza, P. Valente, C. Vicario, Il Nuovo Cim. C 32 (2009) 433.
[22] T. Levato, M. Calvetti, F. Anelli, D. Batani, R. Benocci, L. Cacciotti, C.A. Cecchetti, O. Cerafogli, P. Chimenti, A. Clozza, N. Drenska, A. Esposito, R. Faccini, S. Fioravanti, A. Gamucci, C. Gatti, A. Giulietti, D. Giulietti, L. Labate, V. Lollo, S. Martellotti, M. Monteduro, E. Pace, N.C. Pathak, L. Pellegrino, F. Piastra, M. Pistoni, G.D. Pirro, R.D. Raddo, U. Rotundo, R. Ricci, M. Richetta, C. Vaccarezza, P. Valente, L.A. Gizzi, Nuclear Instruments and Methods in Physics Research Section A: Accelerators, Spectrometers, Detectors and Associated Equipment 720 (2013) 95.
[23] ⟨http://www.baslerweb.com/products/scout.html⟩.
[24] R. Taki, Gas Density Measurements at JAEA, JAEA Internal Report, 2007.
[25] L.A. Gizzi, C.A. Cecchetti, A. Giulietti, D. Giulietti, P. Koester, L. Labate, T. Levato, N. Pathak, IEEE Trans. Plasma Sci. 39 (2011) 2954.
[26] Y. Glinec, J. Faure, A. Guemnie-Tafo, V. Malka, H. Monard, J.P. Larbre, V.D. Waele, J.L. Marignier, M. Mostafavi, Rev. Sci. Instrum. 77 (2006) 103301.
[27] L.A. Gizzi, C. Benedetti, C.A. Cecchetti, G.D. Pirro, A. Gamucci, G. Gatti, A. Giulietti, D. Giulietti, P. Koester, L. Labate, T. Levato, N. Pathak, F. Piastra, Appl. Sci. 3 (2013) 559.
[28] S. Banerjee, S.Y. Kalmykov, N.D. Powers, G. Golovin, V. Ramanathan, N.J. Cunnigham, K.J. Brown, S. Chen, I. Ghebregziabher, B.A. Shadwick, D.P. Umstadter, B.M. Cowan, D.L. Bruhwiler, A. Beck, E. Lefebvre, Phys. Rev. St. Accel. Beams 16 (2013) 031302.
[29] S.P.D. Mangles, A.G.R. Thomas, M.C. Kaluza, O. Lundh, F. Lindau, A. Persson, F.S. Tsung, Z. Najmudin, W.B. Mori, C.-G. Wahlstrom, K. Krushelnick, Phys. Rev. Lett. 96 (2006) 215001.
[30] N.M. Naumova, J. Koga, K. Nakajima, T. Tajima, T.Z. Esirkepov, S.V. Bulanov, F. Pegoraro, Phys. Plasmas 8 (2001) 4149.
[31] K. Nakamura, W. Wan, N. Ybarrolaza, D. Syversrud, J. Wallig, W.P. Leemans, Single-shot electron spectrometer for Gev-class laser-plasma-based accelerators, Rev. Sci. Inst. 79 (5) 053301.
[32] A.H. Lumpkin, Y. Crowell, K. Nemeth, A compact electron spectrometer for an LWFA, in: Proceedings of FEL, 2007, p. 294.
[33] F. Rossi, P. Londrillo, A. Sgattoni, S. Sinigardi, G. Turchetti, Towards robust algorithms for current deposition and dynamic load-balancing in a gpu particle in cell code, in: AIP Conference Proceedings, vol. 1507 (1), 2012, p. 184.
[34] A. Buck, M. Nicolai, K. Schmid, C.M.S. Sears, A. Sävert, J.M. Mikhailova, F. Krausz, M.C. Kaluza, L. Veisz, Real-time observation of laser-driven electron acceleration, Nat. Phys. 7 (2011) 543.
[35] P. Muggli, B. Allen, Y. Fang, V. Yakimenko, M. Babzien, K. Kusche, M. Fedurin, J. Vieira, J. Martins, L. Silva, Three regimes of relativistic beam–plasma interaction, in: AIP Conference Proceedings, vol. 1507, 2012, p. 594.
[36] T. Levato, C.A. Cecchetti, L. Labate, L.A. Gizzi, N. Drenska, R. Faccini, S. Martellotti, F. Tani, C. Gatti, C. Vaccarezza, P. Valente, A. Giulietti, V. Lollo, D. Giulietti, N.C. Pathak, F. Piastra, M. Richetta, Preliminary results of the self-injection test experiment (SITE) at FLAME, in: Proceedings of the International School of Physics Enrico Fermi, vol. 179, pp. 155–161, http://dx.doi.org/10.3254/978-1-61499-129-8-155.